Engineering xxx (xxxx) xxx

Contents lists available at ScienceDirect

Engineering

journal homepage: www.elsevier.com/locate/eng

Research
High Performance Manufacturing—Article

A Comparative Study of Friction Self-Piercing Riveting and Self-Piercing Riveting of Aluminum Alloy AA5182-O

Yunwu Ma [a,b,c], He Shan [a,b], Sizhe Niu [a,b], Yongbing Li [a,b,*], Zhongqin Lin [a,b], Ninshu Ma [c]

[a] Shanghai Key Laboratory of Digital Manufacture for Thin-Walled Structures, School of Mechanical Engineering, Shanghai Jiao Tong University, Shanghai 200240, China
[b] State Key Laboratory of Mechanical System and Vibration, School of Mechanical Engineering, Shanghai Jiao Tong University, Shanghai 200240, China
[c] Joining and Welding Research Institute, Osaka University, Osaka 567-0047, Japan

ARTICLE INFO

Article history:
Received 1 May 2020
Revised 26 May 2020
Accepted 29 June 2020
Available online xxxx

Keywords:
Self-piercing riveting
Friction self-piercing riveting
Mechanical joining
Quasi-static strength
Fatigue

ABSTRACT

In this paper, self-piercing riveting (SPR) and friction self-piercing riveting (F-SPR) processes were employed to join aluminum alloy AA5182-O sheets. Parallel studies were carried out to compare the two processes in terms of joint macrogeometry, tooling force, microhardness, quasi-static mechanical performance, and fatigue behavior. The results indicate that the F-SPR process formed both rivet–sheet interlocking and sheet–sheet solid–state bonding, whereas the SPR process only contained rivet-sheet interlocking. For the same rivet flaring, the F-SPR process required 63% less tooling force than the SPR process because of the softening effect of frictional heat and the lower rivet hardness of F-SPR. The decrease in the switch depth of the F-SPR resulted in more hardening of the aluminum alloy surrounding the rivet. The higher hardness of aluminum and formation of solid-state bonding enhanced the F-SPR joint stiffness under lap-shear loading, which contributed to the higher quasi-static lap-shear strength and longer fatigue life compared to those of the SPR joints.

1. Introduction

The implementation of light alloys in automotive body manufacturing is a strategic approach to improve fuel efficiency. This, together with the lightweight demand of electric vehicle bodies to improve the battery range, has driven automotive manufacturers worldwide to replace traditional steel parts with an increasing amount of aluminum alloys, raising the demand for aluminum spot joining.

Resistance spot welding (RSW) is a high-reliability and low-cost technology extensively used in traditional steel vehicle body assembly. However, the RSW of aluminum alloys faces several critical issues. Aluminum alloys have a higher thermal conductivity, electrical conductivity, specific heat, and latent heat than steel; thus, they require a larger quantity of resistive heating in a shorter time and therefore a much higher welding power requirement than the steel RSW process [1]. Additionally, aluminum RSW is subjected to rapid electrode cap wear due to the nonuniform and nonconducting oxide film on the aluminum surface that generates excessive heat around the electrodes [2]. Another key issue of aluminum RSW lies in the strength loss after welding, i.e., the so-called thermal softening effect, due to the dissolution of precipitates at high welding temperatures [3]. Improved RSW techniques, such as RSW using multi-ring domed (MRD) electrodes [4,5] and the DeltaSpot RSW process using specially designed tapes between the electrode cap and the aluminum workpiece [6], have been proven capable of alleviating oxide film problems and balancing the heat distribution during RSW.

Mechanical fastening methods, such as clinching, self-piercing riveting (SPR) and flow drill screwing (FDS), have been extensively used to fabricate aluminum-intensive vehicle bodies. SPR possesses high joining strength, short cycle time, and no thermal effects [7–9], making it the most preferred alternative to the aluminum RSW process, especially for load-bearing structures in a body-in-white. Numerous studies have been published in the past two decades to investigate the formation and performance of aluminum SPR joints. Xu [10] investigated the effects of rivet and die profiles on the physical attributes of SPR joints. Huang et al. [11] studied the riveting-induced distortion to the SPR joints of AA5182-H11 aluminum alloy sheets. The influences of the clamping force, blank holder size, and sheet width/length on the local distortion of the SPR joint were revealed, and process optimization was conducted to minimize the local distortion. Zhao et al. [12]

* Corresponding author.
E-mail address: yongbinglee@sjtu.edu.cn (Y. Li).

https://doi.org/10.1016/j.eng.2020.06.015

investigated the effects of workpiece thickness on the fatigue performance of SPR joints. They observed a transfer of the fatigue failure position from the upper workpiece to the lower workpiece with increasing sheet thickness. He et al. [13] also reported the transfer of fatigue failure position in an SPR joint as a result of the increased joint stiffness. Zhang et al. [14] pointed out that the fatigue failure of SPR joints was highly relevant to fretting damage, the location of which changed from the interface between the rivet tip and lower sheet to the interface between the upper and lower sheets with a decrease in the load. Li [15] investigated the influence of aluminum surface conditions on the SPR joint strength of AA5754. He reported that grit blasting or sandpaper grounding increased the surface roughness of the aluminum sheet and increased the resistance of rivet slip-out from the lower sheet, which enhanced the lap-shear strength of the aluminum SPR joints.

Research and application of the SPR process in 5xxx and 6xxx series aluminum alloys have already been successfully and comprehensively performed. However, cracking, which deteriorates the joint mechanical performance to a great extent, is inevitable when riveting low ductility metals, such as cast aluminum, 7xxx series aluminum alloys and magnesium alloys, due to the large localized plastic deformation that sheet materials undergo. Preheating of the workpieces via laser [16], resistance heating [17], or induction heating [18] methods before SPR has been adopted to improve the formability of materials and inhibit cracking. However, all these preheating methods require add-on tools and thereby lead to increased process costs and cycle times.

Li et al. [19] invented a friction self-piercing riveting (F-SPR) process to cope with the cracking problem for riveting low-ductility metals. By converting the feeding motion of a rivet during the SPR process into a hybrid motion of feeding and rotating, the F-SPR process generates local frictional heat to soften the surrounding metals. Since the F-SPR process generates heat by the rotation of the rivet, the high cost and long cycle time spent on preheating are eliminated. Liu et al. [20] achieved crack-free joining of magnesium alloy AZ31B and aluminum alloy AA7075-T6 by F-SPR. Ma et al. [21] improved the F-SPR joint performance by introducing a two-stage strategy, which fed the rivet slowly with rapid spinning in the first stage for heat generation and then quickly without spinning in the second stage for rivet flaring. This two-stage strategy successfully improved the lap-shear strength of friction self-piercing riveted aluminum alloy and magnesium alloy joints by 30%. Moreover, as a byproduct of the stir motion of the rivet, solid-state bonding forms at the sheet/sheet interfaces in F-SPR joints, providing another enhancement in addition to mechanical interlocking. Similar combinations of mechanical joining and metallurgical/adhesive bonding were reported by Huang et al. [22,23] and Meng et al. [24] for aluminum-to-steel as well as metal-to-polymer joints.

To date, all the studies published regarding F-SPR have focused on low-ductility materials. It is no doubt that the F-SPR joints in low-ductility materials, where cracking is eliminated, have a better load-bearing capacity than the SPR joints that show visible cracking. However, the comparisons between these two processes are hardly fair. There is a gap in the existing body of work because a comprehensive comparison between SPR and F-SPR processes has not yet been provided.

In this paper, an AA5182-O aluminum alloy, which is not classified as a low ductility metal and can be soundly riveted by the SPR process without cracking, was selected for a back-to-back competition between the SPR and F-SPR processes. Comparisons between the two processes were carried out in terms of joint macro-geometry, tooling force, microhardness, quasi-static mechanical behavior, and fatigue performance.

2. Experimental details

2.1. Materials

Commercial automotive-grade AA5182-O aluminum alloys with thicknesses of 1.5 and 2.0 mm were used as the upper layer (rivet side) and lower layer (die side), respectively. Table 1 presents the mechanical properties of the AA5182-O aluminum alloy.

2.2. Process procedures and parameters

As shown in Fig. 1, the SPR process was performed by punching a semi-hollow rivet against sheet workpieces, which were supported by a matching die. While penetrating through the upper sheet, the rivet shank flared plastically to interlock the workpieces. Pip dies are mainly used for joining soft materials (e.g., 5xxx series aluminum alloy) to increase rivet flaring [25]. In a servo-driven SPR process, the tooling velocity that determines the initial kinetic energy of the rivet is adjusted to control the rivet insertion depth in the workpieces. A flush set down of the rivet head in the upper sheet is always treated as a target for a trial of the tooling velocity [26].

The F-SPR process starts with driving a rivet, rotating it at a high speed, and feeding it slowly in stage I for frictional heat generation and workpiece softening. Then, in stage II, the spinning is stopped and it is fed quickly to achieve rivet flaring, as shown in Fig. 2 [27]. Stages I and II are also known as the friction softening stage and the punch riveting stage, respectively. Therefore, the F-SPR process parameters include two feed rates, one rotational speed, and one switch depth for the two stages. If the two feed rates and rotational speed are fixed, a smaller switch depth results in less friction heat generation and thereby a larger force to flare the rivet shank but raises the risk of material cracking or rivet buckling owing to insufficient softening of the workpieces. In contrast, a larger switch depth corresponds to a higher friction heat generation that is helpful for material softening but at the cost of compromising rivet flaring. If the switch depth is set to zero, the F-SPR process turns into the traditional SPR process.

For a given stack of sheets, various rivet and die combinations can be used to produce an SPR joint, among which an optimum selection is determined via an evaluation of the cross-section geometries. In this study, preliminary work was performed to optimize the rivet and die for the studied sheet stack according to the SPR evaluation indexes in the vehicle industry [28]. The optimized steel countersunk rivet had a hardness of 483 Vickers hardness (HV) and a mass of approximately 0.6 g, as shown in Fig. 3(a). The pip die had a 9.0 mm cavity diameter and 2.0 mm depth, as shown in Fig. 4. A tooling velocity of 220 $mm \cdot s^{-1}$ was used to achieve flush set down of the rivet cap in the upper sheet. The cycle time of the SPR process was approximately 0.05 s.

Fig. 3(b) shows the dimensions of the friction self-piercing rivet. A patented rivet head design was adopted to ensure reliable rotational driving [29]. The rivet head included six equally spaced notches for torque transmission and a center positioning hole. Since the rivet for the F-SPR process had an axisymmetrical body and a nonaxisymmetrical head, the rivet cross-sections may differ in the head profile. Fig. 5 shows the three-dimensional model and three typical cross-sectional profiles of the friction self-piercing rivet. Except for the rivet head design, the other dimensions of the rivet for the F-SPR process were completely comparable to those for SPR. The rivet for F-SPR has a hardness of 255 HV, much softer than the rivets for SPR. The mass of the rivet for the F-SPR process was approximately 0.9 g, which is 50% heavier than that for SPR due to the additional rivet head structures. A pip die with a 9.0 mm cavity diameter and 1.7 mm depth was used for the F-SPR process.

Table 1
Mechanical properties of the AA5182-O aluminum alloy.

Material	Density (kg·m^{-3})	Young's modulus (GPa)	Yield strength (MPa)	Ultimate tensile strength (MPa)	Elongation (%)
AA5182-O	2660	70.9	126	270	26.8

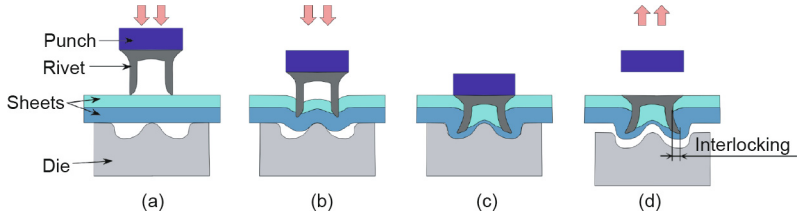

Fig. 1. Schematic of the SPR process. (a) Positioning, (b) rivet piercing the upper sheet, (c) rivet setting down, and (d) tooling retreat.

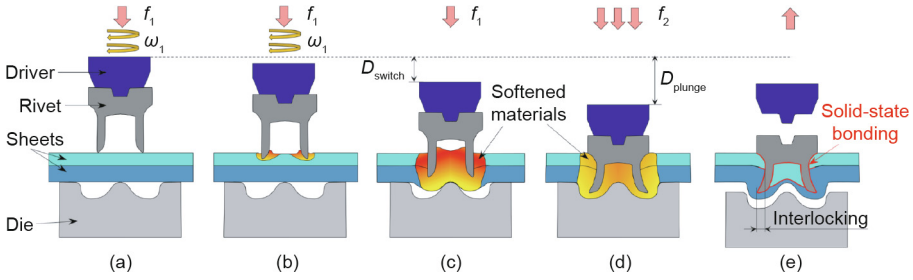

Fig. 2. Schematic of the F-SPR process. (a) Positioning, (b) friction softening, (c) quick stopping, (d) punch riveting, and (e) tooling retreat. f_1, f_2: rivet feed rates of stage I and stage II, respectively; ω_1: rotational speed of stage I; D_{switch}: switch depth; D_{plunge}: constant rivet plunge depth. Reproduced from Ref. [27] with permission of Elsevier, ©2020.

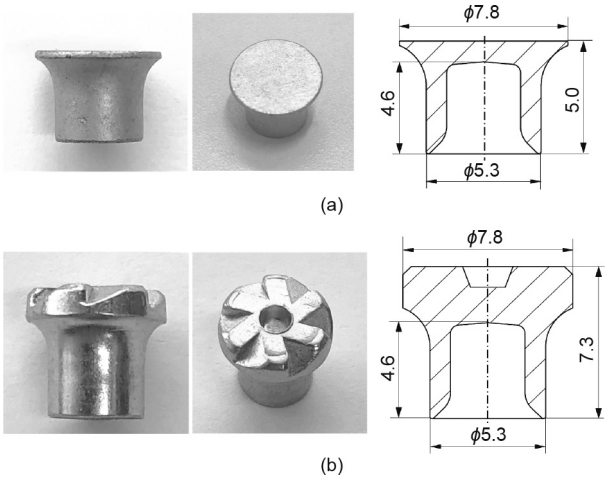

Fig. 3. Physical images and dimensions of the rivets. (a) SPR and (b) F-SPR. The unit is millimeter.

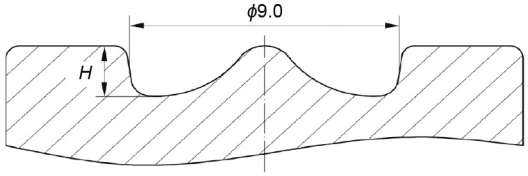

Fig. 4. Dimensions of the pip die in the SPR and F-SPR processes. The unit is millimeter. *H*: die depth.

The F-SPR process was performed on a customized machine equipped with two servo motors, which accounted for the feeding and spinning motions. In all the F-SPR experiments, a constant rivet plunge depth (D_{plunge}) of 5.3 mm was applied. The rivet feed rate (f_1) and rotational speed (ω_1) of stage I and the rivet feed rate (f_2) of stage II were also set as constants, leaving the switch depth (D_{switch}) as the only variable. Table 2 lists the detailed process parameter sets and the corresponding cycle times. An increase in D_{switch} resulted in additional process time being spent on the friction softening of the work materials and therefore a longer total cycle time. When D_{switch} was set equal to D_{plunge}, the process contained only stage I, as shown for F-SPR_1 in Table 2.

The energy input during F-SPR can be quantified as:

$$E = \int_0^{\Delta t} F \times f \mathrm{d}t + \int_0^{\Delta t} M \times \omega \mathrm{d}t \quad (1)$$

where E is the energy input, f is the rivet feed rate, F is the reactive force, M is the reactive torque, t is time, ω is rotational speed, and Δt is the process time. The calculated energy inputs using the measured tooling force and driving torque under various process parameters are listed in Table 2. As expected, the energy input increased with D_{switch}.

2.3. Cross-section observation and microhardness testing

The as-fabricated SPR and F-SPR joints were cross-sectioned, mechanically ground, polished to a surface finish of 0.03 μm, and observed with a Leica DM6M optical microscope (LEICA Microsystems, Germany). Microhardness measurements of aluminum sheet materials around the rivet were conducted on a Wilson VH1102

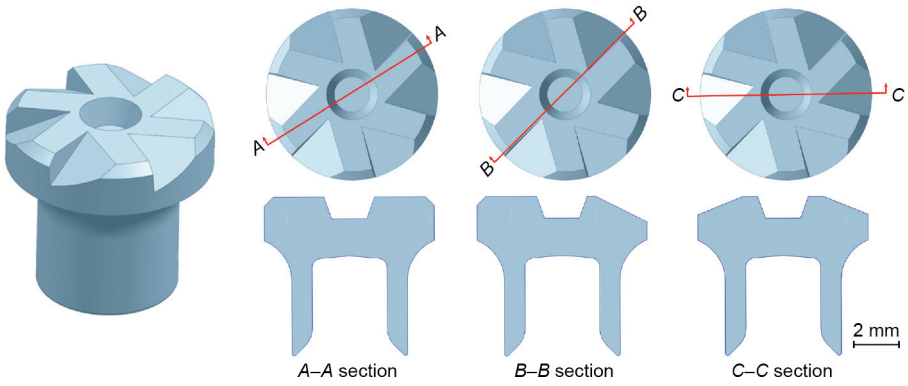

Fig. 5. Three-dimensional model and three typical cross-section profiles of the friction self-piercing rivet.

hardness tester (Buehler, USA) with a 0.2 mm pitch, 50 g load, and 10 s dwell time.

2.4. Mechanical tests

Quasi-static lap-shear tests of the SPR and F-SPR joints were conducted at 3.0 mm·min^{-1} stroke speed on a SUNS UTM5540X tensile machine (SUNS, China). The peak load and energy absorption presented in this paper were averaged from three repetitive tests. Load-controlled fatigue tests were performed for the riveted joints at 20 Hz on a closed-loop MTS servo-hydraulic test frame (MTS Systems Corporation, USA) under tension–tension mode. A sinusoidal waveform with a constant amplitude was applied. The ratio of the minimum load to the maximum load, known as the load ratio R, was 0.1. Termination of the fatigue test was triggered by either the occurrence of visible cracks or the cycle count reaching two million.

The same specimen configuration and grip distance were used during the quasi-static and fatigue tests, as shown in Fig. 6. During the tests, spacers with appropriate thicknesses were attached to both ends of the specimen to avoid undesirable bending effects.

3. Results and discussion

3.1. Joint macroscopic profile and tooling force

Fig. 7 shows the macroscopic profile of of an SPR joint. The rivet shank penetrated through the upper sheet and flared into the lower sheet without any cracking or gap defects, forming a sound joint. An interface was presented between the trapped aluminum and the lower sheet. The rivet flaring of the SPR joint, defined as the diameter of the rivet shank tip in the final joint, was 6.24 mm.

Fig. 8 presents the macroscopic profiles of the F-SPR joint under four different process parameter sets. The joint macroscopic profiles differed significantly for various D_{switch} values. For F-SPR_1, where D_{switch} = 5.3 mm, obvious defects occurred, including a large void close to the rivet tip and a sharp notch at the joint bottom. Moreover, apparent burrs were formed near the flange of the rivet head, as shown in Fig. 8(a). The size of the void at the rivet tip decreased with a reduction in the D_{switch} value and diminished completely at a D_{switch} of 2.0 mm (F-SPR_4), as shown in Fig. 8(d). The sharp notch at the rivet tip and the burrs near the rivet head flange were also eliminated for a D_{switch} smaller than 4.0 mm, as

Table 2
F-SPR process parameter combinations and the corresponding energy inputs.

Process number	Stage I		Stage II		D_{switch} (mm)	D_{plunge} (mm)	Cycle time (s)	Energy input (kJ)
	f_1 (mm·s^{-1})	ω_1 (rpm)	f_2 (mm·s^{-1})	ω_2 (rpm)				
F-SPR_1	2.0	3600	0	0	5.3	5.3	2.65	2.91
F-SPR_2	2.0	3600	11	0	4.0	5.3	2.12	1.88
F-SPR_3	2.0	3600	11	0	3.0	5.3	1.71	1.34
F-SPR_4	2.0	3600	11	0	2.0	5.3	1.30	0.85

rpm: revolutions per minute.

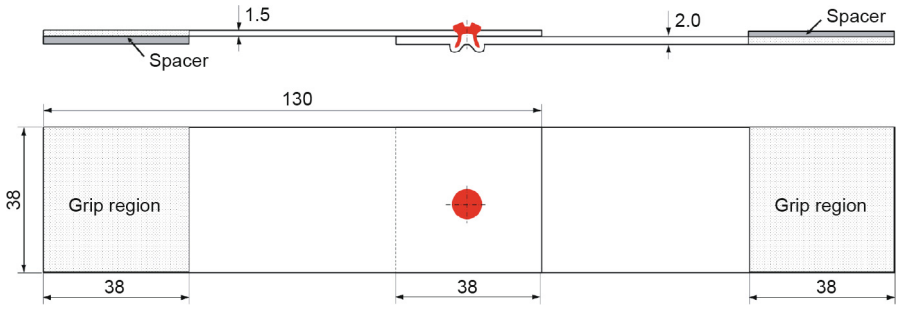

Fig. 6. Dimensions of lap-shear and fatigue testing samples. The unit is millimeter.

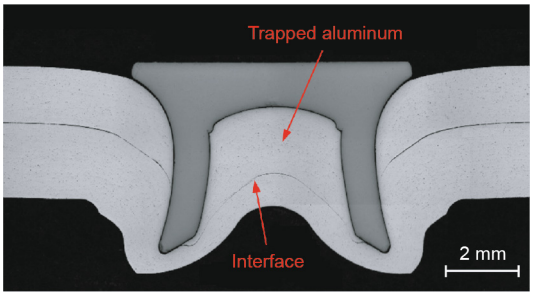

Fig. 7. Macroscopic profile of an SPR joint.

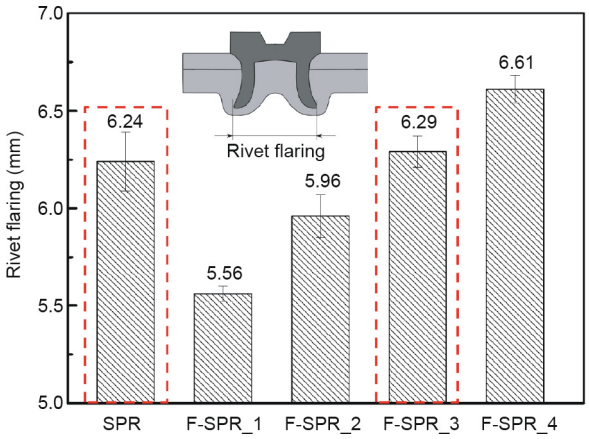

Fig. 9. Rivet flaring of the SPR and the F-SPR joints.

shown in Figs. 8(c) and (d). Moreover, the rivet flaring increased with a reduction in D_{switch}, i.e., from F-SPR_1 to F-SPR_4, as shown in Fig. 9.

The variation of the F-SPR joints with D_{switch} can be explained as follows. The F-SPR process under D_{switch} = 5.3 mm (F-SPR_1), corresponding to the highest heat input among the studied process parameter sets, resulted in an overheating and oversoftening condition of the aluminum adjacent to the rivet. Therefore, less deformation resistance acted on the rivet. The rivet tip only deformed slightly, creating the smallest rivet flaring, as shown in Fig. 9. Moreover, as the oversoftened aluminum surrounding the rivet tip had high fluidity, it flowed almost freely to the die cavity with the feeding of the rivet, leaving a large void at the rivet tip and forming a sharp notch at the joint bottom, as shown in Fig. 8(a). With a reduction in D_{switch}, the generated heat decreased. Consequently, the increased deformation resistance of the aluminum sheets resulted in greater rivet flaring, as shown in Fig. 9. When D_{switch} decreased to 3.0 or 2.0 mm, the heat generation decreased significantly, and the aluminum material was not able to flow freely like it did under a larger D_{switch}; instead, it was pushed by the greatly flared rivet tip and curved down towards the wall of the die cavity. As a result, void and sharp notch defects were eliminated. The curved interfaces in the joints from F-SPR_3 (D_{switch} = 3.0 mm) and F-SPR_4 (D_{switch} = 2.0 mm) support this explanation, as shown in Figs. 8(c) and (d).

The burrs near the rivet head flange in the F-SPR_1 (D_{switch} = 5.3 mm) and F-SPR_2 (D_{switch} = 4.0 mm) joints were produced by the rotational motion of the rivet. In stage I of the F-SPR process, the aluminum materials close to the rivet tip were softened to a high-fluidity condition and squeezed by the rivet shank to flow towards the upper sheet surface, forming burrs. For the F-SPR_3 (D_{switch} = 3.0 mm) and F-SPR_4 (D_{switch} = 2.0 mm) joints, however, the relatively lower heat input and the bending effect of the sheets successfully inhibited the formation of burrs.

It is noteworthy that in all four F-SPR joints, the aluminum interfaces near the rivet outer surface and inside the rivet shank diminished, indicating that solid-state bonding formed between the aluminum alloy sheets, as shown in Fig. 8. The solid-state bonding inside the rivet cavity did not change with the applied F-SPR process parameters. However, the solid-state bonding area outside the rivet decreased with a decrease in D_{switch} due to a reduction in the heat input.

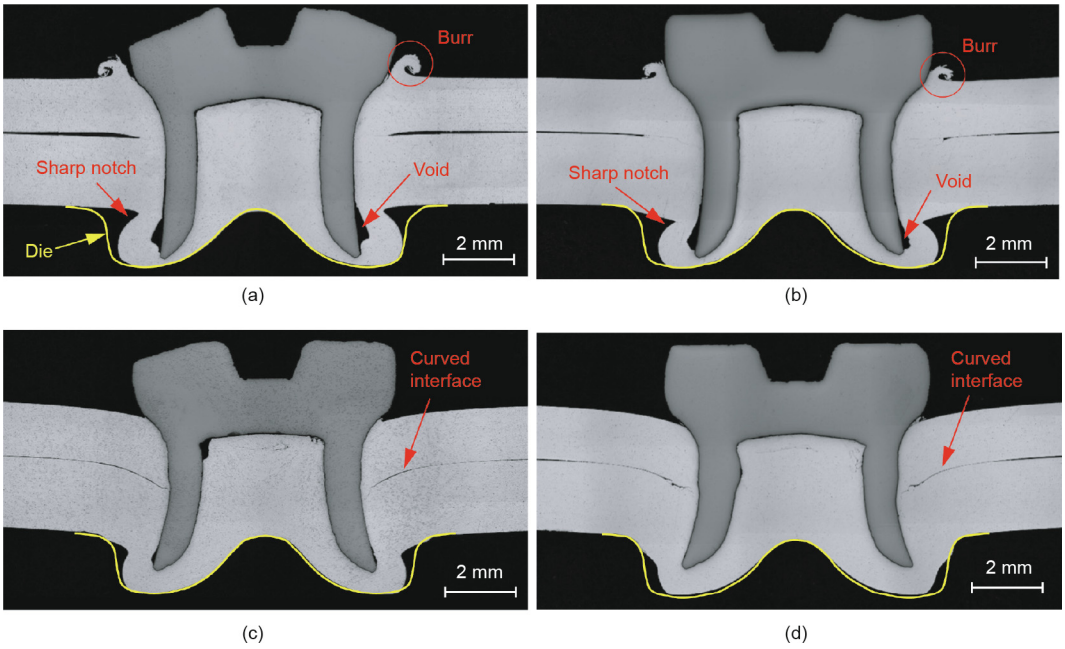

Fig. 8. Macroscopic profiles of the F-SPR joint under four different process parameter sets. (a) F-SPR_1 (D_{switch} = 5.3 mm), (b) F-SPR_2 (D_{switch} = 4.0 mm), (c) F-SPR_3 (D_{switch} = 3.0 mm), and (d) F-SPR_4 (D_{switch} = 2.0 mm).

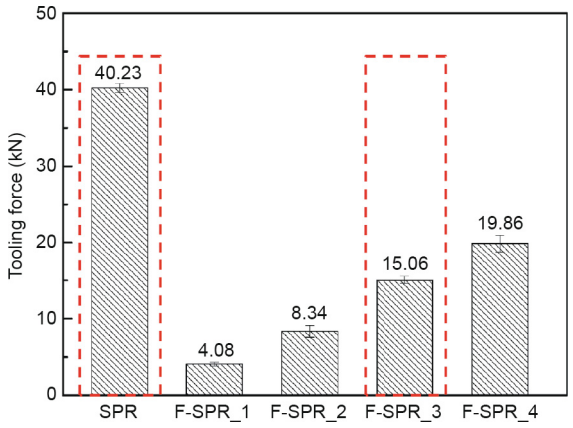

Fig. 10. Peak tooling force of the SPR and F-SPR processes.

Fig. 10 compares the peak tooling forces required to finish the SPR and F-SPR processes. The peak tooling force of the SPR process was more than 40 kN. However, the F-SPR process required more than a 50% lower tooling force. From F-SPR_1 to F-SPR_4, an increase in the peak tooling force was observed with a decrease in D_{switch} owing to the decreased energy input. This increase in tooling force resulted in increased rivet flaring. One can notice that the F-SPR_3 (D_{switch} = 3.0 mm) joint showed a similar rivet flaring but required 63% less tooling force compared to that for the SPR joint, as marked by red dashed boxes in Figs. 9 and 10. This can be attributed to the softening effect of friction heat and the lower rivet hardness of F-SPR. It is noteworthy that the SPR and F-SPR processes have different requirements for rivets to reach the desired rivet flaring. The rivet in the SPR process is subjected to greater resistance from the workpieces. A harder rivet is required to avoid rivet buckling or rivet failure during the SPR process. However, the workpieces in the F-SPR process are softened by friction heat. As a result, the rivet is subjected to less feeding resistance and is less likely to flare during the F-SPR process. Therefore, a softer rivet is necessary for the F-SPR process to achieve the desired rivet flaring. A reduction in the F-SPR tooling force can result in lower wear rates of the riveting tool and the die, lower required C-frame stiffness and lower required capacity of servo motors of the riveting gun, and less residual stress in the joints. All these factors can help reduce the process cost and increase the process reliability.

3.2. Microhardness distribution

In an SPR joint, the workpiece materials adjacent to the rivet are subjected to local work hardening because of the intense plastic deformation. However, in an F-SPR joint, the work materials adjacent to the rivet are subjected to both work hardening and thermal softening, making the strength variation of the work material complex. Fig. 11 shows the microhardness distribution of the workpiece materials in the SPR and the F-SPR joints.

The hardness of the AA5182-O base material is 79 HV. As shown in Fig. 11(a), the aluminum in the SPR joint hardened due to a large plastic deformation. Aluminum located adjacent to the rivet shank and below the rivet tip, where plastic deformation was severe, had a relatively higher hardness. The highest hardness in the SPR joint reached 136 HV. For the F-SPR joint with D_{switch} = 5.3 mm (F-SPR_1), as shown in Fig. 11(b), the aluminum hardness close to the rivet shank and below the rivet tip increased slightly, and the highest hardness was only 98 HV. This is because the high frictional heat input caused material softening, which partially compensated for the work hardening due to plastic deformation. With a decrease in D_{switch}, the thermal softening effect weakened. Moreover, the high-rate feeding of the rivet in stage II of the F-SPR increased the degree of work hardening on the workpiece material. As a consequence, the overall hardness of aluminum sheets increased with a decrease in D_{switch}, referring to Figs. 11 (c)–(e). To this end, it can be concluded that using a small D_{switch} in the F-SPR process is beneficial to alleviate the negative effect of thermal softening.

3.3. Quasi-static mechanical performance

Fig. 12 compares the lap-shear strength and energy absorption of the SPR and F-SPR joints in quasi-static lap-shear tests. As shown in Fig. 12, the F-SPR joint with D_{switch} = 5.3 mm had the lowest strength and energy absorption because of its smallest rivet flaring

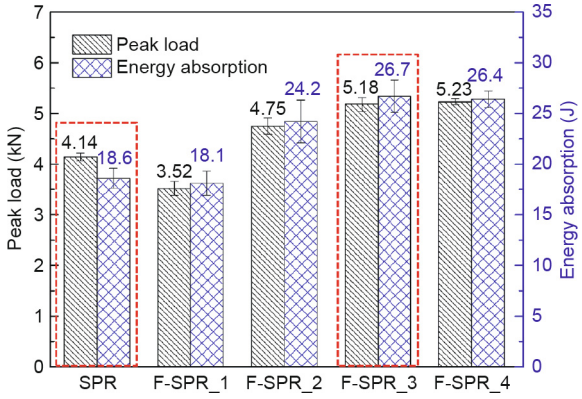

Fig. 12. Lap-shear strength and energy absorption of the SPR and F-SPR joints.

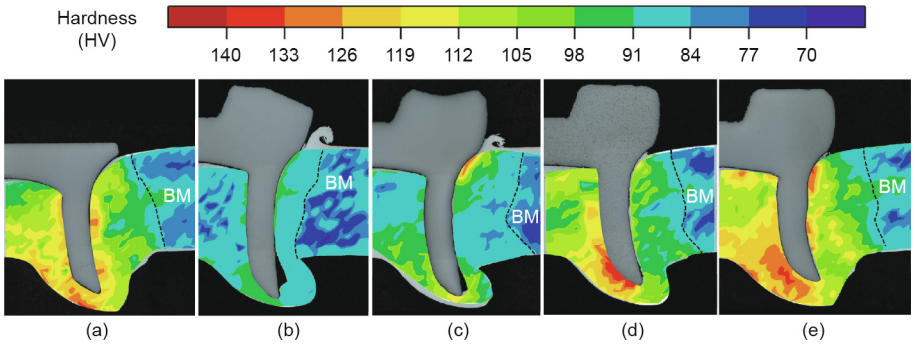

Fig. 11. Microhardness distribution of the workpiece materials in the SPR and F-SPR joints. (a) SPR, (b) F-SPR_1 (D_{switch} = 5.3 mm), (c) F-SPR_2 (D_{switch} = 4.0 mm), (d) F-SPR_3 (D_{switch} = 3.0 mm), and (e) F-SPR_4 (D_{switch} = 2.0 mm). BM: base material.

among all the joints. For the rest of the F-SPR joints, a higher strength and energy absorption than those for the SPR joints were achieved. The joints for F-SPR_3, which had a rivet flaring value similar to that for the SPR joint, showed a 25.1% and 43.5% higher lap-shear strength and energy absorption, respectively, than the SPR joint.

Fig. 13 shows the lap-shear load–displacement curves of the SPR and the F-SPR joint. For the SPR joint and the F-SPR joint with D_{switch} = 5.3 mm (F-SPR_1), yielding occurred earlier, and rivet pull-out mode was presented, as shown in Fig. 14(a). The rest of the F-SPR joints yielded at higher loads, and the corresponding failure mode was upper sheet fracture, as shown in Fig. 14(b). The load–displacement curves from 2.0 to 3.5 kN are magnified and shown in Fig. 13. The joints for F-SPR_2–4 exhibited higher stiffness than the F-SPR_1 and the SPR joints before yielding. The improved strength and stiffness of the F-SPR joints were due to the larger rivet flaring, higher hardness of aluminum surrounding the rivet, and the formation of solid-state bonding. The upper sheet fracture mode indicates that the mechanical interlocking between the rivet and the sheet was strong enough to bear the lap-shear load, and the upper sheet surrounding the rivet became the weakest part of the joint. The occurrence of upper sheet fracture indicates that the strength of the joint almost reached its upper limit.

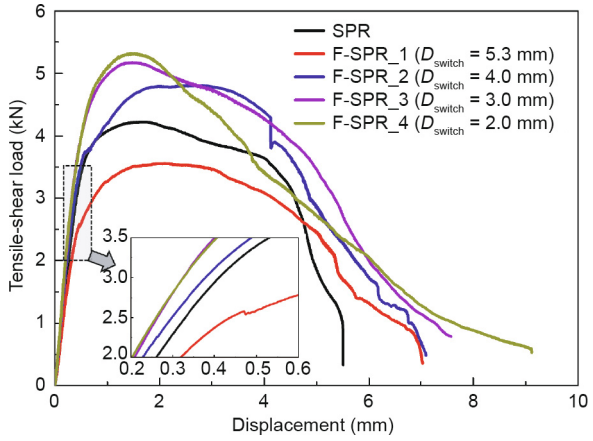

Fig. 13. Lap-shear load–displacement curves of the SPR and the F-SPR joints.

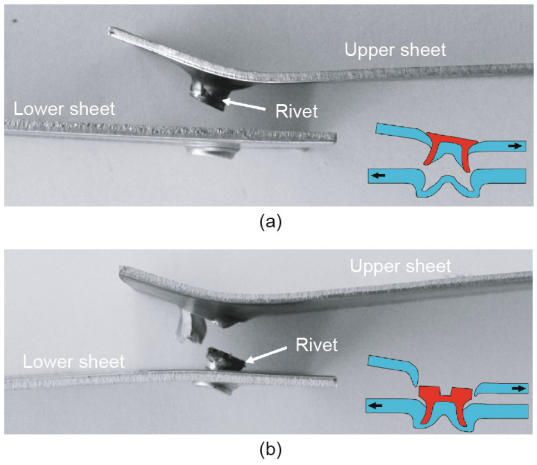

Fig. 14. Lap-shear failure modes of the SPR and the F-SPR joints. (a) Rivet pull-out of the SPR joint and (b) upper sheet fracture of the F-SPR_3 (D_{switch} = 3.0 mm) joint.

3.4. Fatigue performance

Among the four F-SPR joints processed with different parameters, F-SPR_3 had the closest rivet flaring as well as hardness distribution compared to those for the SPR joint. Therefore, F-SPR_3 was selected for comparison of the fatigue performance with the SPR joint. The fatigue results are listed in Table 3 and plotted as the load amplitude (S) versus the number of cycles to failure (N), which are known as S–N curves, as shown in Fig. 15.

From the S–N curves the load amplitudes corresponding to 10^5 fatigue life are calculated to be 2.82 and 3.34 kN for SPR and F-SPR, respectively. Similarly, the load amplitudes corresponding to 10^6 fatigue life are 2.14 and 2.45 kN for SPR and F-SPR, respectively. Therefore, the F-SPR joints presented 18.4% and 14.5% higher load amplitudes for the 10^5 and 10^6 fatigue lives, respectively, compared to those of the SPR joints. For both joints, the fatigue lives were extended with a decrease in the load amplitude. Nevertheless, the F-SPR joint had longer fatigue lives than the SPR joint. The SPR joint with both high (3.0 kN) and low (2.5 kN) load amplitudes and the F-SPR joint with a high load amplitude (3.2 kN) failed in the upper sheet next to the rivet cap, as shown in Figs. 16(a) and (b). However, the F-SPR joint at a low load amplitude (2.7 kN) failed in the lower sheet near the rivet tip, as shown in Figs. 16(c) and (d).

Table 3
Fatigue results of the SPR and F-SPR_3 joints.

Joint type	Load amplitude, S (kN)	Number of cycles to failure, N	Failure location
SPR	3.0	60 552	Upper sheet
		61 935	Upper sheet
		70 770	Upper sheet
	2.5	253 863	Upper sheet
		217 210	Upper sheet
		280 277	Upper sheet
	2.0	1 687 284	Upper sheet
		2 000 000	No failure
		2 000 000	No failure
F-SPR	3.2	182 866	Upper sheet
		143 546	Upper sheet
		216 772	Upper sheet
	2.7	384 535	Lower sheet
		365 506	Lower sheet
		335 741	Lower sheet
	2.2	2 000 000	No failure
		2 000 000	No failure
		2 000 000	No failure

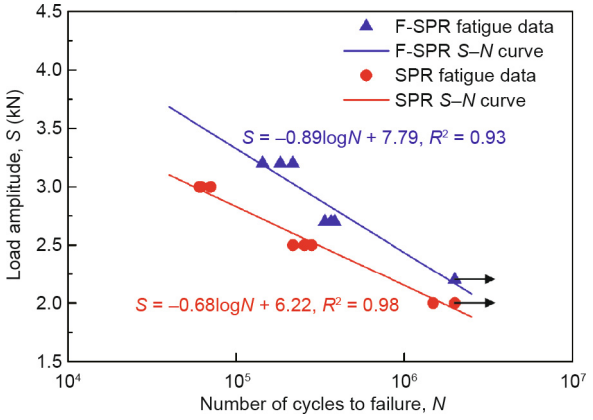

Fig. 15. S–N curves of the SPR and the F-SPR joints. The black arrows indicate that the fatigue test terminated after two million cycles without failure.

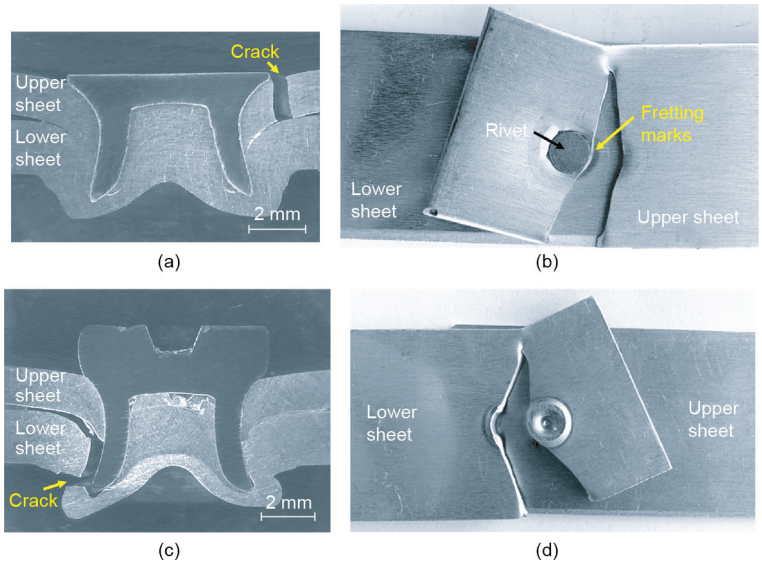

Fig. 16. Crack locations after fatigue tests. (a, b) SPR joint at a 2.5 kN load amplitude and (c, d) F-SPR_3 joint at a 2.7 kN load amplitude.

A similar upper sheet fatigue failure location in the aluminum SPR joint was reported by Li et al. [30]. The upper sheet failure mode was attributed to the occurrence of cyclic secondary bending, which resulted in a stress concentration near the rivet head and further accelerated fretting damage as well as the development of fatigue cracks in the upper sheet. In this study, the secondary bending of the upper sheet was greater due to its reduced thickness compared to that of the lower sheet. As a result, fretting occurred at the interface between the two sheets, as demonstrated by the area with dark fretting debris marks in Fig. 16(b). The SPR joint with a 2.5 kN load amplitude corresponded to less secondary bending compared to that for a 3.0 kN load amplitude; therefore, the number of cycles was increased before fatigue failure.

Fig. 17 presents the fracture surfaces of the SPR joint at a 2.5 kN load amplitude. As shown in Fig. 17, the central region, roughly underneath the rivet cap, exhibited cleavage fracture. The typical cleavage steps in Fig. 17(b) corresponded to brittle transgranular fracture, indicating the initiation of fatigue cracks adjacent to the rivet cap. The region near the sheet edge exhibited dimple fracture, as shown in Fig. 17(c), which is indicative transient ductile fracture when a local stress exceeds the bearing limit of the remaining structure. To this end, the fracture path in the upper sheet can be conjectured as being from a crack initiating in the region near the rivet cap due to fretting wear and propagating along the sheet width direction until complete fracture.

Similarly, the F-SPR joint at a load amplitude of 3.2 kN also failed in the upper sheet due to fretting damage. The F-SPR joint exhibited a higher stiffness than the SPR joint, as indicated by the shorter displacement of the F-SPR_3 joint at a 3.2 kN lap-shear load than the SPR joint with a 3.0 kN load, as shown in Fig. 13. Therefore, less secondary bending was induced in the F-SPR joint under the cyclic fatigue load, resulting in a larger number of cycles before fatigue failure.

For the F-SPR joint at a 2.7 kN load amplitude, the decrease in the load amplitude reduced the bending effect and changed the fracture location from the upper sheet to the lower sheet. Fig. 18 shows the microstructures on the surface of the rivet shank and the fractured lower sheet. Due to fretting wear in the faying

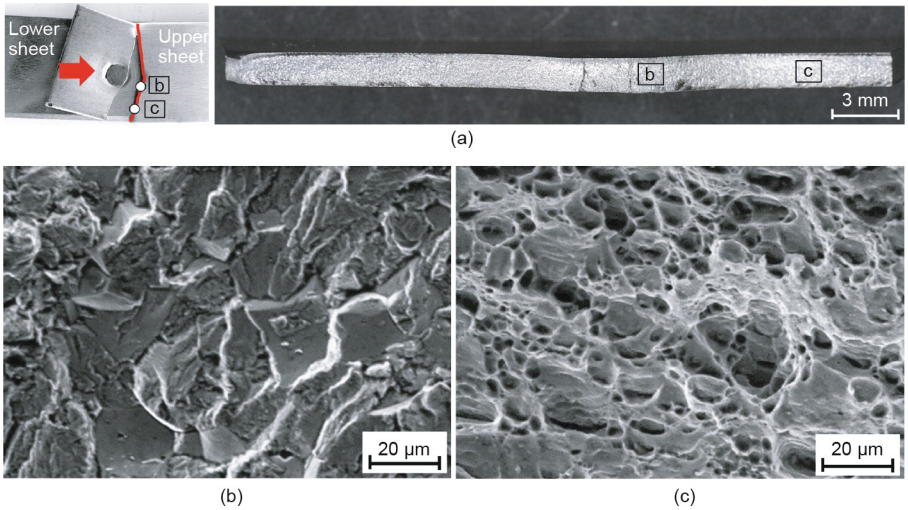

Fig. 17. Fracture surfaces of the SPR joint at a 2.5 kN load amplitude. (a) Magnified view of the fracture surface of the upper sheet, (b) scanning electron microscope (SEM) image of location b in (a) showing transgranular fracture, and (c) SEM image of location c in (a) showing ductile fracture.

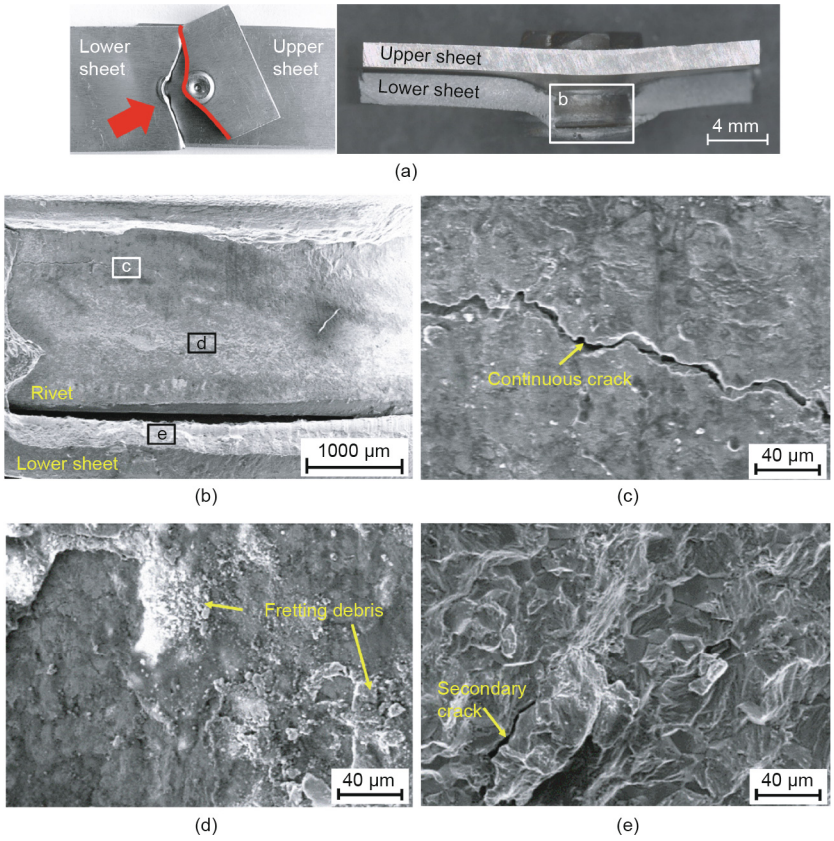

Fig. 18. Fracture surfaces of the F-SPR_3 joint at a 2.7 kN load amplitude. (a) Close-up view of the fractured sample; (b) SEM image of location b in (a) showing the rivet surface and lower sheet; (c, d) SEM images of locations c and d in (b) showing crack and fretting debris on the rivet surface, respectively; and (e) SEM image of location e in (b) showing transgranular fracture in the lower sheet.

interface between the rivet and the lower sheet, the materials on the sheet surface were scratched, oxidized, and stuck to the rivet shank. Moreover, local fretting also caused cracking of the rivet shank. Therefore, the rivet shank that contacted the lower sheet exhibited a continuous crack and a rough surface covered with fretting debris, as shown in Figs. 18(c) and (d). On the fracture surface of the lower sheet near the rivet tip in Fig. 18(e), transgranular fracture with secondary cracks and fatigue striations were present, indicating the propagation of fatigue cracks in this region. Thus, the fatigue failure of the F-SPR joint was due to the fretting between the rivet and the lower sheet, which caused the fatigue crack to develop in the lower sheet near the rivet tip and propagate along the thinnest area at the joint bottom where a notch was present, as shown in Fig. 19.

Although the F-SPR_3 and the SPR joints had a similar rivet flaring, the stronger stiffness of the F-SPR_3 joint enhanced the resistance to secondary bending during the fatigue test, which delayed the fretting damage in the upper sheet. However, the presence of a notch at the F-SPR joint bottom became a short slab, hindering the further improvement of the high cycle fatigue performance. In future work, process optimization is necessary to eliminate the notch in the F-SPR joint and increase the wall thickness of the lower sheet surrounding the rivet tip.

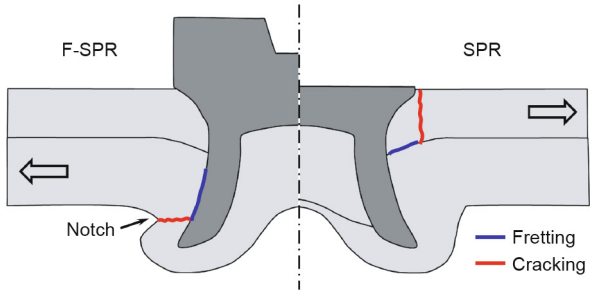

Fig. 19. Fretting and cracking locations in the F-SPR and the SPR joints at low load amplitudes.

4. Conclusions

This body of work applied both SPR and F-SPR processes to join 1.5-mm-thick to 2.0-mm-thick AA5182-O aluminum alloy sheets. Comparative studies were carried out to systematically evaluate the two processes in terms of joint macrogeometry, tooling force, microhardness distribution, quasi-static lap-shear performance, and fatigue behavior. The following conclusions can be drawn:

(1) The SPR joint was formed by rivet–sheet interlocking, whereas the F–SPR joint contained both rivet-sheet interlocking and sheet–sheet solid–state bonding. The F-SPR joint created with a 3.0-mm switch depth exhibited a similar rivet flaring but required 63% lower tooling force compared to that for the SPR joints because of frictional heat softening and the lower F-SPR rivet hardness.

(2) The F-SPR joint exhibited an increased aluminum hardness with decreasing switch depth. The F-SPR joint made with switch depths smaller than 4.0 mm increased the hardening of the aluminum surrounding the rivet, which compensated for the softening due to the heat effect and produced a higher overall hardness than that in the SPR joints.

(3) Due to the higher hardness of aluminum and the formation of solid-state bonding, the F-SPR joint with a 3.0 mm switch depth exhibited a 25.1% and 43.5% higher lap-shear strength and energy absorption, respectively, compared to those for the SPR joint.

(4) The higher stiffness of the joint alleviated secondary bending under a cyclic tensile load, which delayed the fretting damage in the upper sheet and improved the load amplitudes by 18.4% and 14.5% for 10^5 and 10^6 fatigue lives, respectively, compared to those for the SPR joint.

(5) The F-SPR process required a cycle time that was 0.8–2.9 s longer than that for the SPR process and approximately 0.3 g of rivet weight addition due to the rotational driving structures on the rivet head. Future studies for the F-SPR process may focus on improving the process efficiency and lightweight design of rivets.

Acknowledgements

The authors would like to acknowledge the financial support of the National Natural Science Foundation of China (52025058 and U1764251) and the National Key Research and Development Program of China (2016YFB0101606-8).

Compliance with ethics guidelines

Yunwu Ma, He Shan, Sizhe Niu, Yongbing Li, Zhongqin Lin, and Ninshu Ma declare that they have no conflict of interest or financial conflicts to disclose.

References

[1] Manladan SM, Yusof F, Ramesh S, Fadzil M, Luo Z, Ao S. A review on resistance spot welding of aluminum alloys. Int J Adv Manuf Technol 2017;90(1–4):605–34.
[2] Luo Z, Ao S, Chao YJ, Cui X, Li Y, Lin Y. Application of pre-heating to improve the consistency and quality in AA5052 resistance spot welding. J Mater Eng Perform 2015;24(10):3881–91.
[3] Zohoori-Shoar V, Eslami A, Karimzadeh F, Abbasi-Baharanchi M. Resistance spot welding of ultrafine grained/nanostructured Al 6061 alloy produced by cryorolling process and evaluation of weldment properties. J Manuf Process 2017;26:84–93.
[4] Sigler DR, Carlson BE, Janiak P. Improving aluminum resistance spot welding in automotive structures. Weld J 2013;92(6):64–72.
[5] Deng L, Li Y, Carlson BE, Sigler DR. Effects of electrode surface topography on aluminum resistance spot welding. Weld J 2018;97(4):120–32.
[6] Trommer G. Resistance spot welding using continuous tape. Weld J 2009;88:12.
[7] Mori K, Abe Y, Kato T. Self-pierce riveting of multiple steel and aluminium alloy sheets. J Mater Process Technol 2014;214(10):2002–8.
[8] Jiang H, Gao S, Li G, Cui J. Structural design of half hollow rivet for electromagnetic self-piercing riveting process of dissimilar materials. Mater Des 2019;183:108141.
[9] Hirsch F, Müller S, Machens M, Staschko R, Fuchs N, Kästner M. Simulation of self-piercing rivetting processes in fibre reinforced polymers: material modelling and parameter identification. J Mater Process Technol 2017;241:164–77.
[10] Xu Y. Effects of factors on physical attributes of self-piercing riveted joints. Sci Technol Weld Join 2006;11(6):666–71.
[11] Huang H, Du D, Chang BH, Sui B, Chen Q. Distortion analysis for self-piercing riveting of aluminium alloy sheets. Sci Technol Weld Join 2007;12(1):73–8.
[12] Zhao L, He X, Xing B, Lu Y, Gu F, Ball A. Influence of sheet thickness on fatigue behavior and fretting of self-piercing riveted joints in aluminum alloy 5052. Mater Des 2015;87:1010–7.
[13] He X, Zhao L, Deng C, Xing B, Gu F, Ball A. Self-piercing riveting of similar and dissimilar metal sheets of aluminum alloy and copper alloy. Mater Des 2015;65:923–33.
[14] Zhang X, He X, Gu F, Ball A. Self-piercing riveting of aluminium–lithium alloy sheet materials. J Mater Process Technol 2019;268:192–200.
[15] Li D. Influence of aluminium sheet surface modification on the self-piercing riveting process and the joint static lap shear strength. Int J Adv Manuf Technol 2017;93(5–8):2685–95.
[16] Durandet Y, Deam R, Beer A, Song W, Blacket S. Laser assisted self-pierce riveting of AZ31 magnesium alloy strips. Mater Des 2010;31:S13–6.
[17] Wang JW, Liu ZX, Shang Y, Liu AL, Wang MX, Sun RN, et al. Self-piercing riveting of wrought magnesium AZ31 sheets. ASME J Manuf Sci Eng 2011;133(3):031009.
[18] Jäckel M, Grimm T, Landgrebe D. Approaches for mechanical joining of 7xxx series aluminum alloys. AIP Conf Proc 2016;1769(1):100010.
[19] Li Y, Wei Z, Wang Z, Li Y. Friction self-piercing riveting of aluminum alloy AA6061-T6 to magnesium alloy AZ31B. ASME J Manuf Sci Eng 2013;135(6):061007.
[20] Liu X, Lim YC, Li Y, Tang W, Ma Y, Feng Z, et al. Effects of process parameters on friction self-piercing riveting of dissimilar materials. J Mater Process Technol 2016;237:19–30.
[21] Ma Y, He G, Lou M, Li Y, Lin Z. Effects of process parameters on crack inhibition and mechanical interlocking in friction self-piercing riveting of aluminum alloy and magnesium alloy. ASME J Manuf Sci Eng 2018;140(10):101015.
[22] Huang Y, Huang T, Wan L, Meng X, Zhou L. Material flow and mechanical properties of aluminum-to-steel self-riveting friction stir lap joints. J Mater Process Technol 2019;263:129–37.
[23] Huang Y, Meng X, Xie Y, Li J, Wan L. New technique of friction-based filling stacking joining for metal and polymer. Compos Part B Eng 2019;163:217–23.
[24] Meng X, Huang Y, Xie Y, Li J, Guan M, Wan L, et al. Friction self-riveting welding between polymer matrix composites and metals. Compos Part A Appl Sci Manuf 2019;127:105624.
[25] Haque R. Quality of self-piercing riveting (SPR) joints from cross-sectional perspective: A review. Arch Civil Mech Eng 2018;18:83–93.
[26] Ma Y, Lou M, Li Y, Lin Z. Effect of rivet and die on self-piercing rivetability of AA6061-T6 and mild steel CR4 of different gauges. J Mater Process Technol 2018;251:282–94.
[27] Ma Y, Yang B, Lou M, Li Y, Ma N. Effect of mechanical and solid-state joining characteristics on tensile-shear performance of friction self-piercing riveted aluminum alloy AA7075-T6 joints. J Mater Process Technol 2020;278:116543.
[28] Li D, Han L, Thornton M, Shergold M. Influence of edge distance on quality and static behaviour of self-piercing riveted aluminium joints. Mater Des 2012;34:22–31.
[29] Li Y, Ma Y, Lou M, Lin Z, inventors; Shanghai Jiao Tong University, assignee. Rivet for friction self-piercing riveting and friction self-piercing riveting connection system thereof. US patent US 20190039119A1. 2019 Feb 7.
[30] Li D, Han L, Thornton M, Shergold M. Influence of rivet to sheet edge distance on fatigue strength of self-piercing riveted aluminium joints. Mater Sci Eng A 2012;558:242–52.